Available online at www.sciencedirect.com
SCIENCE DIRECT®
Journal of Power Sources 138 (2004) 101–110
JOURNAL OF POWER SOURCES
www.elsevier.com/locate/jpowsour

A 3D model for PEM fuel cells operated on reformate

Tianhong Zhou, Hongtan Liu*

Department of Mechanical Engineering, College of Engineering, University of Miami, P.O. Box 248294, Coral Gables, FL 33124-0624, USA

Received 15 May 2004; accepted 11 June 2004
Available online 23 August 2004

Abstract

A three-dimensional mathematical model for PEM fuel cells operated on reformate is developed based on our previous established fuel cell model [Int. J. Transport Phenomena 3 (2001) 177], by incorporating the adsorption and oxidation kinetics of CO on platinum surface proposed by Springer et al. [Proceedings of the Electrochemical Society, Montreal, Canada, 1997; J. Electrochem. Soc. 148 (2001) A11]. This model is capable of studying the effect of CO poisoning as well as the hydrogen dilution effect by inert gases. The adsorption and oxidation kinetics of CO on a platinum surface are incorporated in the source terms of the species equations; thus, the basic form of the mathematical equations are the same as those used for PEM fuel cells operated on pure hydrogen. With this model, we can obtain detailed information on the CO poisoning and variation of CO and hydrogen concentrations inside the anode. The results from this 3D model reveal many new phenomena that cannot be obtained from previous 1D or 2D models. Results of the effects of various operating and design parameters, such as anode flow rate, gas diffuser porosity, gas diffuser thickness, and the width of the collector plate shoulder, are also presented. The modeling results demonstrate the value of this model as a design and optimization tool for the anode of PEM fuel cells operating on reformate.

Keywords: PEM fuel cells; Fuel cell modeling; Reformate; CFD

1. Introduction

In hydrogen PEM fuel cells, when pure hydrogen is used as the fuel, usually very low polarization occurs at the anode due to the fast hydrogen oxidation. Thus the overpotential at the anode is often neglected in fuel cell models [4–6]. If reformate is used as the fuel for PEM fuel cell, the dilution effect of the inert gases at the anode can no longer be neglected. More importantly, traces of carbon monoxide (CO) are inevitably present in the reformed gases and it can cause substantial poisoning of the catalyst and lead to drastic degradation of fuel cell performance [7]. CO affects the reactivity of the catalyst mainly by preventing H_2 adsorption as the CO molecules adsorb strongly on the active sites of the catalyst surface [8]. This site exclusion behavior of CO, combined with the dilution effect due to decreased hydrogen partial pressure in the anode channel, can cause significant cell voltage losses. These losses, when added to the losses at the cathode, can reduce the fuel cell efficiency to an unusable level. Ways to reduce the CO poisoning effects include internal cleanup methods, such as oxygen bleeding and other oxidation means [9], using catalyst material resistant to the poisoning [10], and adopting operation techniques that can improve CO tolerance [11]. Other research includes studies on the mechanism of CO poisoning [12–16] and the CO tolerance [17,18]. The performance data from PEMFC operated on reformed gas can be found in Refs. [20,21]. The kinetic model presented by Springer et al. [2,3] succeeded in explaining many features of the CO adsorption and reaction during the PEMFC operation. To account for the changing of CO inside the fuel cell chamber, Zhang et al. [21] presented a CO inventory model, which used the basic mass balance between the inlet and outlet to calculate the consumption of CO inside the fuel cell. Though, this model calculated the CO mole fractions at the anode feed and the anode outlet, it neglected

* Corresponding author. Tel.: +1 305 284 2019; fax: +1 305 284 2580.
E-mail address: hliu@miami.edu (H. Liu).

0378-7753/$ – see front matter © 2004 Elsevier B.V. All rights reserved.
doi:10.1016/j.powsour.2004.06.033

Nomenclature

$(ai_0^{\mathrm{ref}})_a$	reference exchange current density times area at anode (A/m^3)
$(ai_0^{\mathrm{ref}})_c$	reference exchange current density times area at cathode (A/m^3)
A_E	effective activate surface area per unit volume of the catalyst layer (m^2/m^3)
b_{fc}	back-to-forward CO adsorption ratio (atm)
b_{fh}	back-to-forward H_2 adsorption ratio (atm)
c	mole concentration of the gas mixture (mol/m^3)
c_{H^+}	proton mole concentration (mol/m^3)
c_p	specific heat at constant pressure (J/kg K)
D_k	binary diffusion coefficient of the k'th component (m^2/s)
E	fuel cell voltage (V)
E_0	open circuit potential (V)
F	Faraday constant, 96 487 (C/mol)
i	current density (A/m^2)
i_{CO}	local kinetic current density from CO (A/m^2)
i_h	local kinetic current density from hydrogen (A/m^2)
j	transfer current density (A/m^3)
k	thermal conductivity (W/m K)
k_{ec}	pre-exponential of CO Tafel electro-oxidation rate (A/m^2)
k_{eh}	pre-exponential of H_{ad} Tafel electro-oxidation rate (A/m^2)
k_{fc}	electrode forward H_2 adsorption rate times 2F (A/cm^2 atm)
k_{fh}	electrode forward CO adsorption rate times 2F (A/m^2 atm)
k_h	hydraulic permeability of the porous layer (m^2)
k_φ	electrokinetic permeability (m^2)
l_{ct}	catalyst layer thickness (m)
P	pressure (Pa)
Q	heat generation rate of the energy equation
$r^{(2)}$	correction factor in the momentum equations for the porous media
R	universal gas constant (8.314 J/mol K)
S_k	source term of the species transport equation
T	temperature (K)
V	velocity vector (m/s)
X	mole fraction

Greek letters

η	electrode overpotential (V)
ε	porosity
μ	viscosity (kg/m s)
ϕ	membrane phase potential (V)
ρ	density (kg/m^3)
σ	ionic conductivity (Ω^{-1} m^{-1})
θ_{CO}	fractional CO coverage of Pt surface
θ_h	fractional coverage of Pt surface, hydrogen

Subscripts

a	anode
c	cathode, CO
ct	catalyst layer
eff	effective
h	hydrogen
i	inlet
k	k'th component
m	membrane
p	porous media

Superscripts

a	anode, anodic
c	cathode, cathodal
ref	reference

the variation of CO concentration along the anode flow direction as well as in across-the-channel direction. In addition, the changing of hydrogen concentration across the fuel cell and along the flow direction was not taken into account.

In this paper, the kinetic equations for the CO adsorption and oxidation behavior provided by Springer et al. [2] is incorporated into our previously established 3D model to study the CO poisoning effect in a fuel cell. In addition, the dilution effect by the inert gases is also included. With this model, we can obtain a detailed variation of CO and hydrogen concentrations inside the anode. Unlike the previous models [2,3,21], the variation of the chemical reaction inside the fuel cell is fully accounted. The modeling results also compared very well with the experimental data by Divisek et al. [19].

2. Mathematical model

Fig. 1 is the schematic of the model geometry of a single fuel cell. The details of the general 3D model can be found

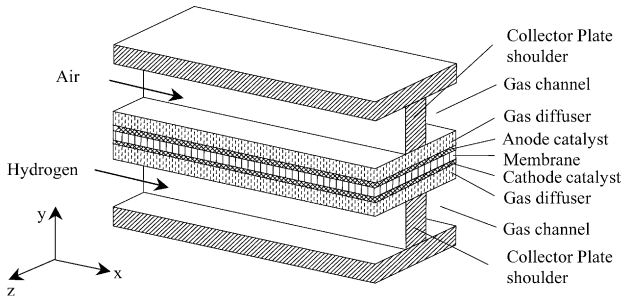

Fig. 1. The schematic of the model geometry of a single fuel cell.

in Zhou and Liu [1]. A summary of the model equations is provided below:

Continuity equation:

$$\nabla(\rho\mathbf{V}) = 0 \tag{1}$$

Momentum equation:

$$\rho\mathbf{V}(\nabla\mathbf{V}) = -\nabla\mathbf{P} + \begin{cases} \mu\nabla^2\mathbf{V} & \text{gas channel} \\ r^{(2)}\mu\nabla^2\mathbf{V} - \frac{\varepsilon\mu}{k_p}\mathbf{V} & \text{gas diffuser} \\ r^{(2)}\mu\nabla^2\mathbf{V} - \frac{\varepsilon\mu}{k_p}\mathbf{V} + \varepsilon c_{H^+}\frac{Fk_\phi(\nabla\phi)}{k_p} & \text{catalyst layer and membrane} \end{cases} \tag{2}$$

Species equation:

$$\rho\mathbf{V}(\nabla X_k) = \varepsilon\rho D_{\text{eff}}\nabla^2 X_k + \begin{cases} 0 & \text{gas channel and gas diffuser} \\ \varepsilon\rho S_k & \text{catalyst layer} \end{cases} \tag{3}$$

Energy equation:

$$\rho c_p\mathbf{V}(\nabla T_k) = k_{\text{eff}}\nabla^2 T_k + \begin{cases} 0 & \text{gas channel and gas diffuser} \\ Q & \text{catalyst layer and membrane} \end{cases} \tag{4}$$

The correction parameters $r^{(2)}$, D_{eff} are defined as [23]:

$$r^{(2)} = 2.25\frac{(1-\varepsilon)^2}{\varepsilon^2} \tag{5}$$

$$D_{\text{eff}} = \begin{cases} D_k & \text{gas channel} \\ D_k\varepsilon^{1.5} & \text{porous media} \end{cases} \tag{6}$$

$$k_{\text{eff}} = \begin{cases} k_{\text{gas}} & \text{gas channel} \\ -2k_p + \frac{1}{\varepsilon/(2k_p+k_{\text{gas}})+(1-\varepsilon)/3k_p} & \text{porous media} \end{cases} \tag{7}$$

At the cathode, the mass generation source term S_k, for oxygen, water, and protons are $j_c/(4Fc)$, $-j_c/(2Fc)$, and $j_c/(Fc)$, respectively. At the anode, the source terms for hydrogen molecules and protons are $-j_a/(2Fc)$, and $j_a/(Fc)$, respectively. The volumetric current generation rates, j_a and j_c, are calculated from Butler–Volmer expression:

$$j_a = (ai_0^{\text{ref}})_a\left(\frac{c_{H_2}}{c_{H_2\text{ref}}}\right)^{1/2} \times\left[\exp\left(\frac{\alpha_a^a F}{RT}\eta_a\right) - \exp\left(-\frac{\alpha_c^a F}{RT}\eta_a\right)\right] \tag{8}$$

$$j_c = (ai_0^{\text{ref}})_c\left(\frac{c_{O_2}}{c_{O_2\text{ref}}}\right) \times\left[\exp\left(\frac{\alpha_a^c F}{RT}\eta_c\right) - \exp\left(-\frac{\alpha_c^c F}{RT}\eta_c\right)\right] \tag{9}$$

The heat source Q is given by,

$$Q = \begin{cases} \frac{j\eta_a + i^2}{\sigma_{ct}} & \text{anode catalyst layer} \\ \frac{i^2}{\sigma_m} & \text{membrane} \\ \frac{j\eta_c + i^2}{\sigma_{ct}} & \text{cathode catalyst layer} \end{cases} \tag{10}$$

The membrane phase potential satisfies:

$$\nabla(\sigma\nabla\eta) = \begin{cases} j_c & \text{cathode catalyst layer} \\ 0 & \text{membrane} \\ j_a & \text{anode catalyst layer} \end{cases} \tag{11}$$

Then the cell voltage is determined by:

$$E = E_0|\eta_c| - |\eta_a| - \int_m \frac{i}{\sigma_m}\,\mathrm{d}y - \int_{ct,a}\frac{i}{\sigma_{ct}}\,\mathrm{d}y - \int_{ct,c}\frac{i}{\sigma_{ct}}\,\mathrm{d}y \tag{12}$$

where E_0 is the open circuit potential. In this paper, the correlation obtained by Gurau et al. [22] from the experimental data of Parthasarathy et al. [23] is used for the specific operation conditions listed in Table 1:

$$E_0 = 0.0025T + 0.2329 \tag{13}$$

Note that generally E_0 depends on pressure as well as temperature, but in this study, all the cases have the same operating pressure. In Eq. (12), the values of the integrals depends on x and z since current density is a function of x and z, in addition to y. In determining the cell voltage, the average value of each integral is used, thus inexplicitly taking into account of the current re-distributions in GDL on the x–z plane.

In the presence of CO at the anode, part of the catalyst surface is covered by CO that causes site exclusion and electron capture through dipole interactions. The value of $(ai_0^{\text{ref}})_a$ used in Eq. (8) is then reduced. Spring et al. [2,3] suggested that, in the presence of CO, the interfacial kinetics of PEMFC using reformate could be represented by four processes:

(1) CO adsorption:

$$\text{CO} + \text{Pt} \underset{b_{fc}k_{fc}}{\overset{k_{fc}}{\rightleftarrows}} (\text{Pt}-\text{CO}) \tag{14}$$

(2) Dissociative chemisorption of hydrogen:

$$\text{H}_2 + 2\text{Pt} \underset{b_{fh}k_{fh}}{\overset{k_{fh}}{\rightleftarrows}} 2(\text{Pt}-\text{H}) \tag{15}$$

(3) Electrochemical oxidation of hydrogen:

$$(\text{Pt}-\text{H}) \xrightarrow{k_{eh}} \text{H}^+ + \text{e}^- + \text{Pt} \tag{16}$$

Table 1
Base-case electrode parameters and properties[a]

Gas channel length, 8.0×10^{-2} m
Gas channel height, 8.0×10^{-4} m
Gas diffuser thickness, 2.0×10^{-4} m
Catalyst layer thickness, 0.3×10^{-4} m
Gas channel width, 10×10^{-4} m
Collector plate shoulder width, 10×10^{-4} m
Membrane thickness, 2.3×10^{-4} m
Gas diffuser porosity, $\varepsilon = 0.4$
Membrane porosity, $\varepsilon_m = 0.28$
Volume fraction of membrane in catalyst layer, $\varepsilon_{mc} = 0.5$
Permeability to air of the gas diffuser, $k_p = 1.76 \times 10^{-11}$ m^2
Hydraulic permeability of membrane, $k_m = 1.58 \times 10^{-18}$ m^2
Reference exchange current density times area at the cathode, $(ai_0^{ref})_c = 5 \times 10^2$ A/m^3
Oxygen reference concentration, 3.39 mol/m^3
Hydrogen reference concentration, 56.4 mol/m^3
Air inlet pressure, 3 atm
Air inlet velocity, 3 m/s
Air inlet temperature, 82 °C
Oxygen/nitrogen ratio in dry air at inlet, 0.21/0.79
Cathode Reynolds number = 347.68
Anode inlet pressure, 3 atm
Anode inlet velocity, 3 m/s
Anode inlet temperature, 82 °C
Anode Reynolds number = 175.78
Anode inlet composition on dry base: 60% H_2, 40% N_2/CO_2, 50 ppm CO
Ionic conductivity of membrane, $\sigma_m = 10\,\Omega^{-1}$ m^{-1}
Reference exchange current density times area at the cathode, $(ai_0^{ref})_a = 5 \times 10^8$ A/m^3
Effective area per unit volume of the catalyst layer $A_E = 50\,000$ m^2/m^3
Back-to-forward CO adsorption ratio, $b_{fc} = 2 \times 10^{-5}$ atm[b]
Back-to-forward H_2 adsorption ratio, $b_{fh} = 0.5$ atm[b]
Electrode forward H_2 adsorption rate times 2F, $k_{fc} = 2.4 \times 10^5$ A/(m^2 atm)[b]
Electrode forward CO adsorption rate times 2F, $k_{fh} = 40\,000$ A/(m^2 atm)[b]
Pre-exponential CO Tafel electro-oxidation rate, $k_{ec} = 10^{-2}$ A/m^2[b]
Pre-exponential H_{ad} Tafel electro-oxidation rate, $k_{eh} = 5000$ A/m^2[b]

[a] Most data from Gurau et al. [22] and Zhou and Liu [1].
[b] From or adapted from Springer et al. [3].

(4) Electrochemical oxidation of CO to CO_2:

$$H_2O + (Pt - CO) \xrightarrow{k_{ec}} Pt + CO_2 + 2H^+ + 2e^- \quad (17)$$

According to Springer et al. [2,3], the first two processes occur simultaneously to compete for the vacant catalyst surface. The third equation represents the current generation by the anodic oxidation of hydrogen and the fourth corresponds to the electrochemical oxidation of CO to CO_2, which reaches significant rate only at high anode overpotential. The poisoning effect of CO is mainly due to the chemical reaction represented by Eq. (14). Due to this process, the part of the Pt surface that adsorbs CO is unavailable for the chemical reaction represented by Eq. (15) and subsequent process by Eq. (16). At large anode overpotentials, the chemical reaction represented by Eq. (17) will reach a significant level. Thus CO will be consumed and part of the CO-adsorbed Pt surface will then be freed.

Under steady-state assumptions, Springer et al. [2] solved the CO and hydrogen adsorption/desorption equilibrium equations and obtained the local generated ionic current densities as:

$$i_h = 2k_{eh}\theta_h \sinh\left(\frac{\eta_a}{b_h}\right) \quad (18)$$

$$i_{CO} = 2k_{ec}\theta_{CO}\, e^{\eta_a/b_c} \quad (19)$$

where $b_h = 2RT/F$ and $b_c = 2RT/F$.

Then the transfer current j_a within the anode catalyst layer becomes:

$$j_a = a_a(i_h + i_{CO}) \quad (20)$$

At the anode, the consumptions of hydrogen and CO are:

$$\frac{-A_E i_h}{2Fc}, \qquad \frac{-A_E i_{CO}}{2Fc} \quad (21)$$

where A_E is the effective active catalyst surface area per unit volume of the catalyst layer.

As the current is mainly from the anode to the cathode, the components of the current along the x and z axes (Fig. 1)

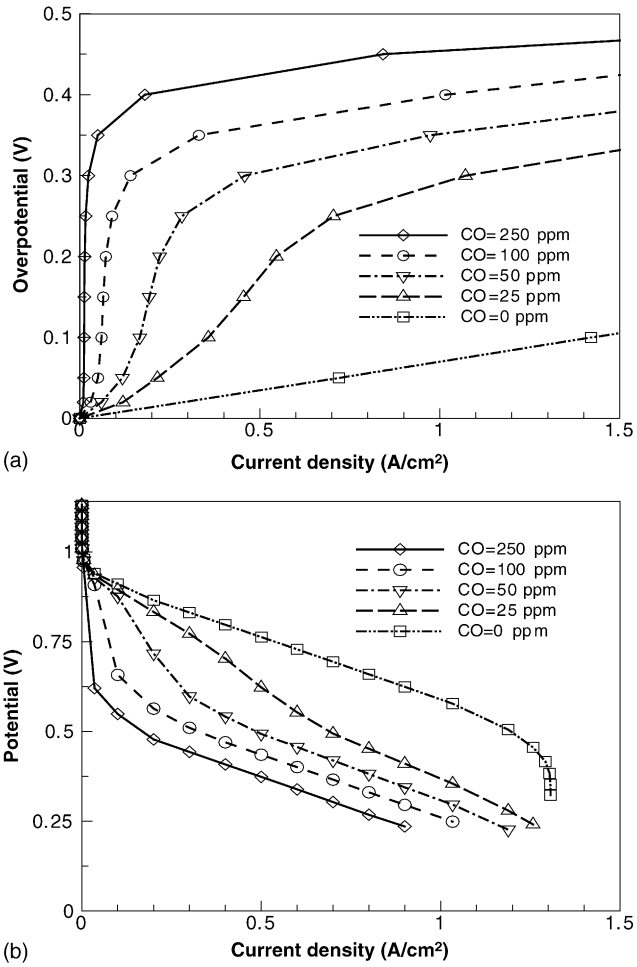

Fig. 2. Modeling results with varied CO content. (a) current density vs. overpotential (b) polarization curve. Case conditions: anode flow is fully saturated reformed gases, with 60% hydrogen, 40% N_2/CO_2 on dry base, flow velocity = 1 m/s, temperature = 82 °C, pressure = 3 atm.

are neglected, and we have,

$$\frac{\partial i}{\partial y} = a_a(i_h + i_{CO}) \quad \text{at anode} \tag{22}$$

Because $i = \sigma(\partial\eta/\partial y)$ and no protons pass through the interface between the GDL and the catalyst layer, thus:

$$\frac{\partial \eta}{\partial y} = 0 \tag{23}$$

Assuming constant overpotential along the interface between the catalyst layer and the membrane, we have:

$$\eta = \eta_a \tag{24}$$

For the above mathematical model, inlet flow conditions are prescribed at the gas channel inlets. The boundary conditions for the species transport equations include the Neumann conditions prescribed along the gas channel walls as well as along the interface between the catalyst layer and the membrane. For the energy equation, constant temperatures along the gas channel outer walls are used to simulate bath cooling. Finally, between the different layers within the fuel cell, continuity is assumed at the interfaces. With a computer program developed in-house [1], the governing equations in the different regions of the fuel cell are solved simultaneously to ensure the coupling of the flow, species, overpotential and current density.

3. Computational results and discussions

A series of computation simulations were performed using the 3D fuel cell model. The base case data and parameter values are listed in Table 1.

Fig. 2(a) shows the modeling results of anode overpotential changes with different current densities at different inlet CO concentrations, and Fig. 2(b) shows the corresponding polarization curves. From Fig. 2(a), it is seen that there is substantial overpotential at the anode when even a very

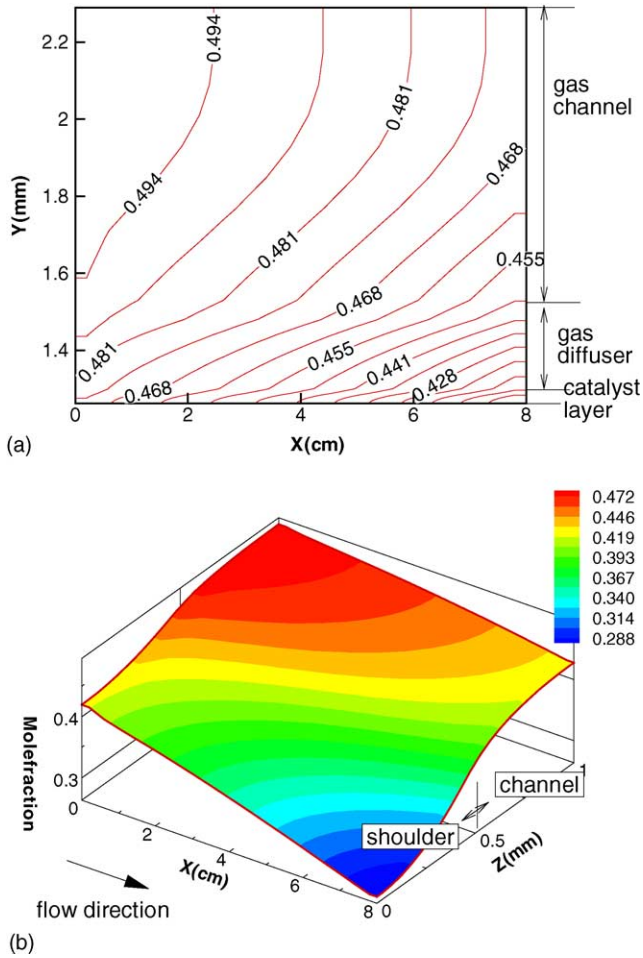

Fig. 3. Hydrogen mole fractions along (a) flow direction (b) across flow direction. Case conditions: anode flow is fully saturated reformed gases, with 60% hydrogen, 40% N_2/CO_2 on dry base, flow velocity = 1 m/s, temperature = 82 °C, pressure = 3 atm, average current density = 0.64 A/cm^2, anode stoichiometric ratio = 3.39.

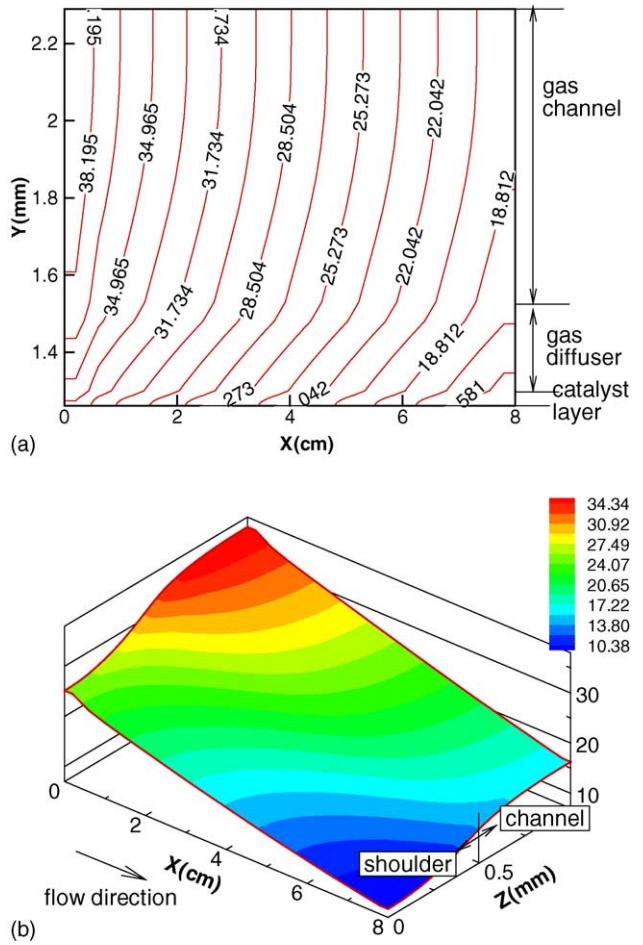

Fig. 4. CO mole fractions along (a) flow direction (b) across flow direction. Case conditions: anode flow is fully saturated reformed gases, with 60% H_2, 40% N_2/CO_2, 50 ppm CO on dry base, flow velocity = 1 m/s, temperature = 82 °C, pressure = 3 atm, average current density = 0.64 A/cm^2, anode stoichiometric ratio = 3.39.

small amount of CO is present. The larger the CO content is, the greater is the anode overpotential. As a result, the fuel cell performance degrades drastically as shown by the polarization curves in Fig. 2(b). From Fig. 2(a), it is also seen that at low current densities the CO poison effect is not as significant. This CO-tolerance exists because only a small portion of the catalyst surface is needed to generate the currents. At such low current densities, the reduction of the active area of the catalyst layer does not have significant effect on the rate of hydrogen oxidation yet, due to the very fast hydrogen oxidation kinetics. As current density increases, more active area of the catalyst surface is needed. Then the reduction of the active area due to CO-adsorption by the Pt surface has significant effect on the rate of hydrogen oxidation. To compensate for the CO-covered catalyst surface, larger activation loss at the anode incurs as shown by Fig. 2(a). This rapid increase of overpotential continues until a certain level when the rate of this increase is reduced. At this point, the CO oxidization reaches a significant level and the consumption of CO releases some CO-covered Pt. Eventually the curves in Fig. 2(b) become parallel, indicating that the absorption and oxidation of CO reach equilibrium.

Fig. 3(a) and (b) are the typical concentration contours of hydrogen mole fraction along the flow direction and across the fuel cell. Fig. 4(a) and (b) are the corresponding CO concentration contours. Along the flow direction, as CO and hydrogen is oxidized, CO and hydrogen concentrations are reduced. A comparison of the local current densities of i_h and i_{CO} shows that i_h is far larger than i_{CO}. This indicates that CO oxidation affects the PEMFC performance through the release of Pt surface that is previously covered by CO, while the contribution of the current density generated by the CO oxidation is negligible.

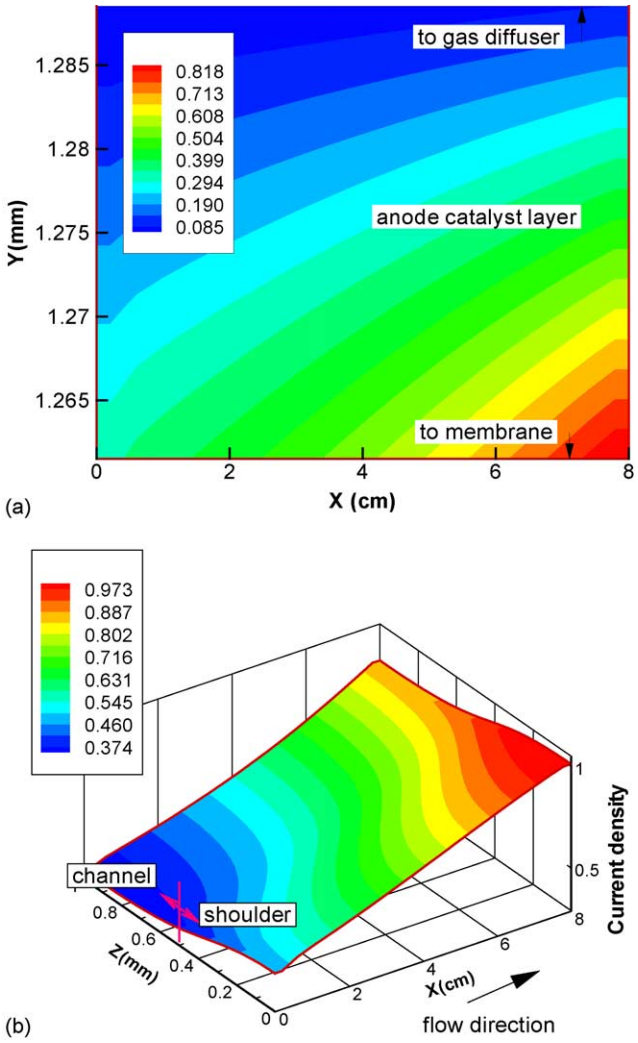

Fig. 5. Local current density along (a) flow direction (b) across flow direction. Case conditions: anode flow is fully saturated reformed gases, with 60% H_2, 40% N_2/CO_2, 50 ppm CO on dry base, flow velocity = 1 m/s, temperature = 82 °C, pressure = 3 atm, average current density = 0.64 A/cm^2, anode stoichiometric ratio = 3.39.

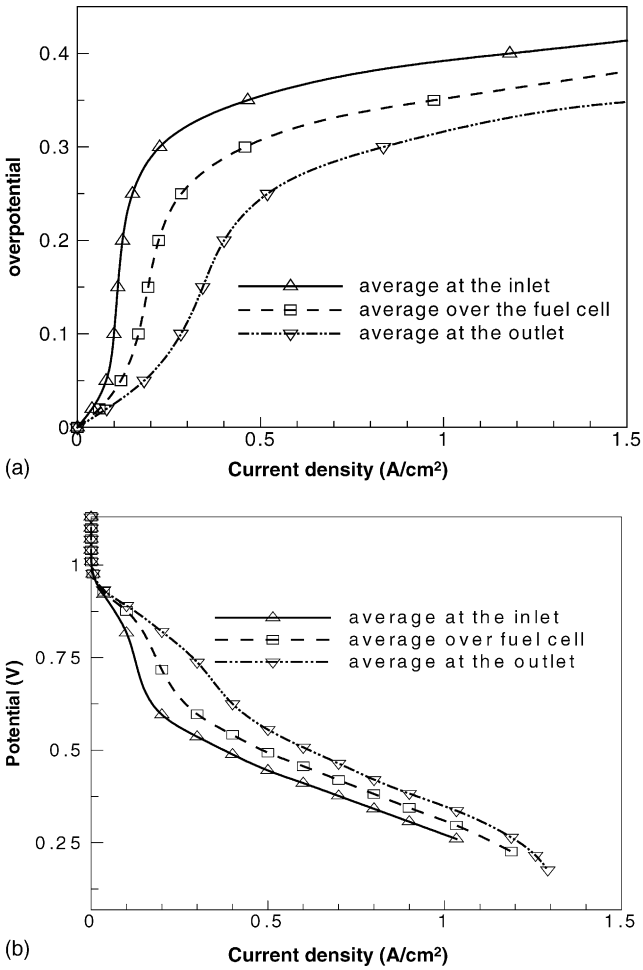

Fig. 6. Current density vs. overpotential and polarization curves when the current densities are averaged at the fuel cell inlet, outlet and whole fuel cell chamber. Case conditions: anode flow is fully saturated reformed gases, with 60% H_2, 40% N_2/CO_2, 50 ppm CO on dry base, flow velocity = 1 m/s, temperature = 82 °C, pressure = 3 atm.

A new phenomenon from the 3D modeling effort is that, due to the reduction of CO, near the exit of the fuel cell, the chemical reaction rate is actually greater than that near the inlet. This is obviously not the case for a fuel cell operated on pure hydrogen. This phenomenon is shown by the local current density distribution in Fig. 5(a) and (b). Near the exit, though hydrogen concentration is reduced due to reaction consumption, the fast oxidation of hydrogen makes the influence of reduced hydrogen concentration negligible. On the other hand, the lower CO concentration down the flow channel due to CO oxidation reduces the poisoning effect and leads to higher current density. To see this reduction effect of CO poisoning more clearly, the relationships between current density and anode overpotentials at the inlet and outlet are plotted in Fig. 6(a) and compared with the average value for the cell. The corresponding polarization curves averaged at the inlet and the outlet as well as for the whole cell are plotted in Fig. 6(b).

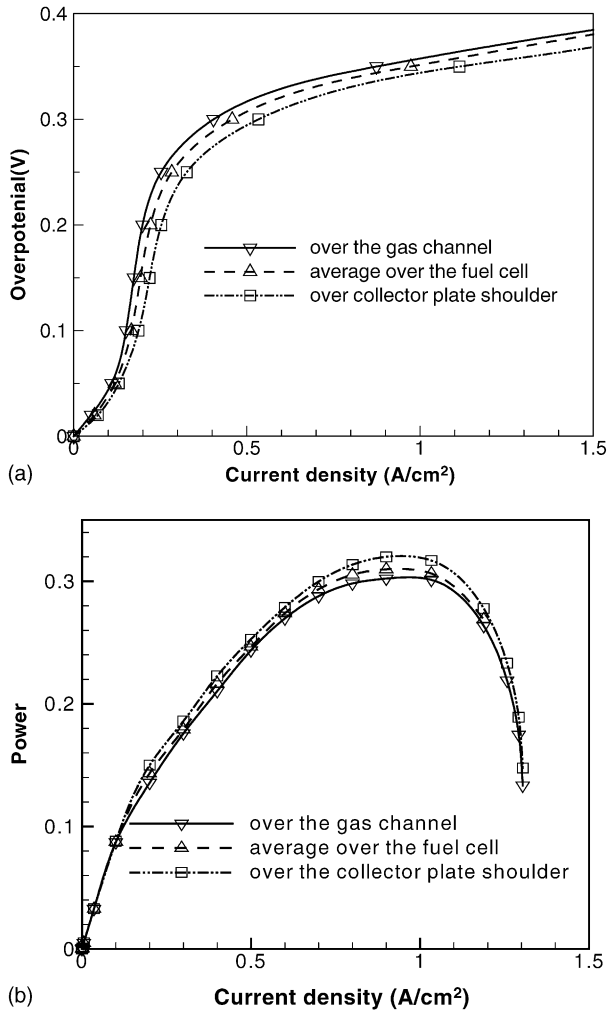

Fig. 7. Current density vs. overpotential and power output vs. current density when the current densities are averaged at regions over the shoulder, over the channel and the whole fuel cell chamber. Case conditions: anode flow is fully saturated reformed gases, with 60% H_2, 40% N_2/CO_2, 50 ppm CO on dry base, flow velocity = 1 m/s, temperature = 82 °C, pressure = 3 atm.

Another interesting new phenomenon is that, over the collector plate shoulder, the chemical reaction is actually greater than that over the flow channel. This result is again different from what was true for a fuel cell using pure hydrogen. Under the collector plate shoulder, both the concentrations of CO and hydrogen are lower. As the mass diffusivity of CO is lower than that of hydrogen, over the collector plate shoulder, the reduced poisoning effect of CO is predominant over the effect of hydrogen concentration reduction. This phenomenon is shown in Fig. 7(a) and (b). Fig. 7 shows anode overpotentials and power densities averaged over the collector plate shoulder and over the gas channel, compared with the averaged values over the cell. This result demonstrates that the shoulder widths of the collector plate at the anode side should be wider for fuel cells using reformate than those using pure hydrogen.

A comparison of the results from 1D and 3D model are shown in Fig. 8. In the 1D model, as the variation of CO content is neglected and an overestimation of CO poisoning effect results.

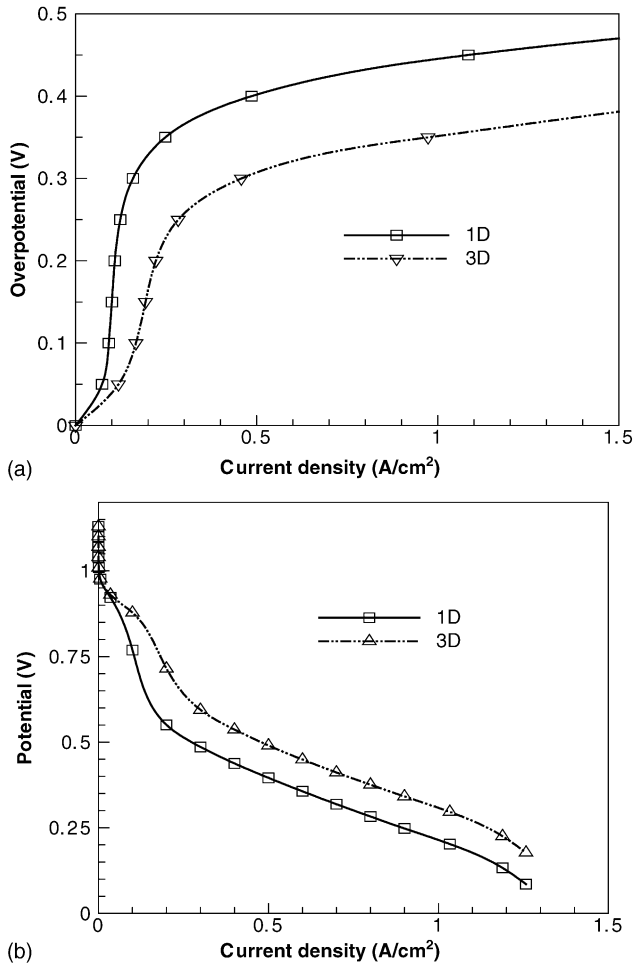

Fig. 8. Comparison of modeling results with 1D and 3D models. (a) current density vs. overpotential (b) polarization curve. Base case conditions: anode flow is fully saturated reformed gases, with 60% H_2, 40% N_2/CO_2, 50 ppm CO on dry base, flow velocity = 1 m/s, temperature = 82 °C, pressure = 3 atm.

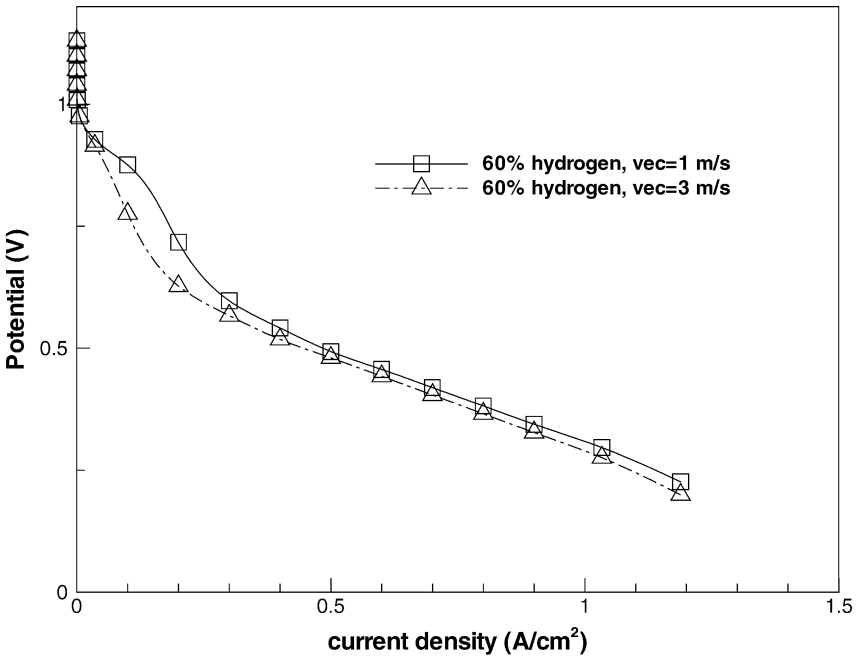

Fig. 9. Polarization curves at different anode flow velocities. Case conditions: anode flow is fully saturated reformed gases, with 60% H_2, 40% N_2/CO_2, 50 ppm CO on dry base, temperature = 82 °C, pressure = 3 atm.

Fig. 9 shows the results of a fuel cell performance at different anode flow velocities. The fuel cell performance is much worse at higher anode flow velocity. Generally speaking fuel cell performance increases with increasing stoic ratio, i.e. flow rate, especially at the cathode. For fuel cell using reformate as the fuel, higher flow rate at anode will bring in more CO as well as more hydrogen. Since under certain conditions, the effects of more CO can overshadow the effect of more hydrogen, the resulting fuel cell performance can decrease with the increase of anode flow rate. Fig. 9 shows such an example, where the anode flow velocity increases from 1 to 3 m/s while all other conditions remain the same, the fuel cell performance decreases considerably. Therefore, under certain conditions, reducing the flow velocity at the anode can be beneficial. This phenomenon is similar to what was discovered by Zhang et al. [21]. However, there is also a limit to this flow rate reduction benefit. If the anode flow rate is too low, the limit current density will be reduced as

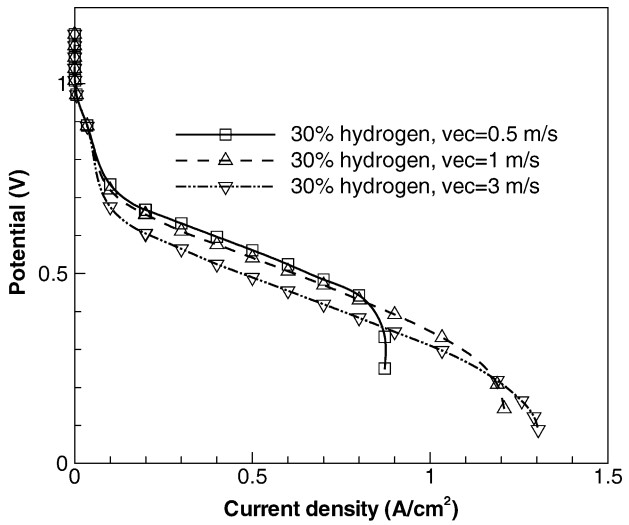

Fig. 10. Polarization curves with varied anode flow velocities. Case conditions: anode flow is fully saturated reformed gases, with 30% H_2, 70% N_2/CO_2, 50 ppm CO on dry base, temperature = 82 °C, pressure = 3 atm.

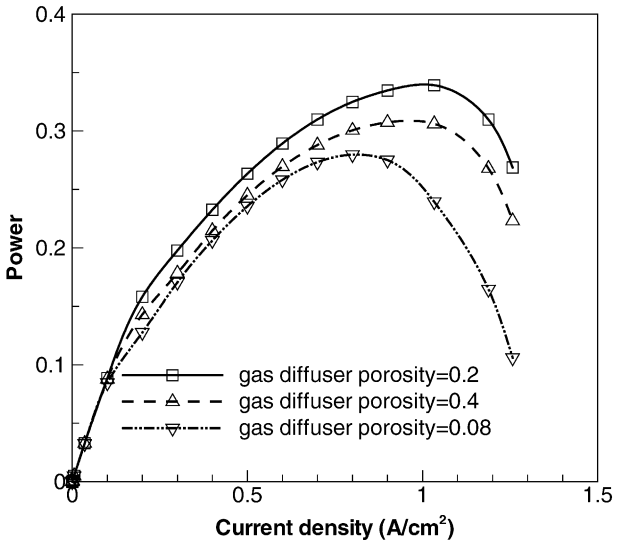

Fig. 11. Power output vs. current density with different gas diffuser porosities. Case conditions: anode flow is fully saturated reformed gases, with 60% H_2, 40% N_2/CO_2, 50 ppm CO on dry base, flow velocity = 1 m/s, temperature = 82 °C, pressure = 3 atm.

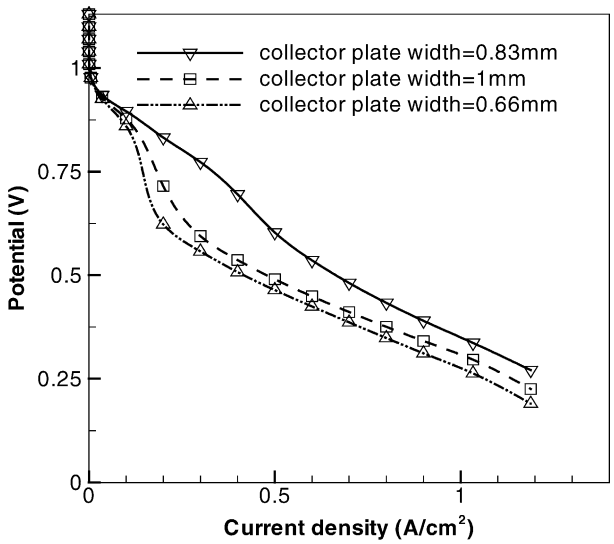

Fig. 12. Polarization curves with different width of the collector plate shoulder at anode. Case conditions: anode flow is fully saturated reformed gases, with 60% H_2, 40% N_2/CO_2, 50 ppm CO on dry base, flow velocity = 1 m/s, temperature = 82 °C, pressure = 3 atm.

shown in Fig. 10. In Fig. 10, the reformed gas contains only 30% hydrogen. The anode flow velocity is 3, 1 and 0.5 m/s, respectively. Under such conditions, as the hydrogen supply is already very low and its further reduction leads to reduced limit current density.

Beside the anode flow velocity, parameters that affect the CO poisoning include the porosity of the anode gas diffuser and the width of the collector plate shoulder. While the cathode side benefits from narrower shoulder and higher gas diffuser porosity due to reduced the mass transport resistance, same may not be true for the anode side. Fig. 11 shows the power density of fuel cell with three different effective porosities of the anode gas diffuser. When the porosity is reduced from 0.4 to 0.2, the anode overpotential is reduced and better performance is achieved, but there is a limit to this reduction. If the porosity is too low, the diffusion rate of hydrogen to the reaction sites will be very limited and the fuel cell performance will decrease, as shown in an extreme case in Fig. 11 when gas diffuser porosity is only 0.08.

Fig. 12 shows the modeling results with different collector plate shoulder widths at the anode. For fuel cells using pure hydrogen, the wider the shoulder, the lower the performance, due to the increased mass transfer resistance. For fuel cells using reformate with traces of CO, the increased shoulder width will lead to lower CO concentration in the catalyst layer and better performance. Similar to the case with gas diffuser porosity, there is a limit to this increase. If the shoulder is too wide, the diffusion rate of hydrogen to the catalyst layer above the collector plate shoulder will be too low and the fuel cell performance will decrease, as shown in Fig. 12.

It is obvious that the optimal design and operating parameters for a fuel cell using reformate could be very different from those for fuel cells using pure hydrogen. For a given case, a careful study should be performed to select the optimal values.

Finally, a comparison between the modeling results and the fuel cell performance data presented by Divisek et al. [19] is plotted in Fig. 13, where the computational results compared well with the experimental data.

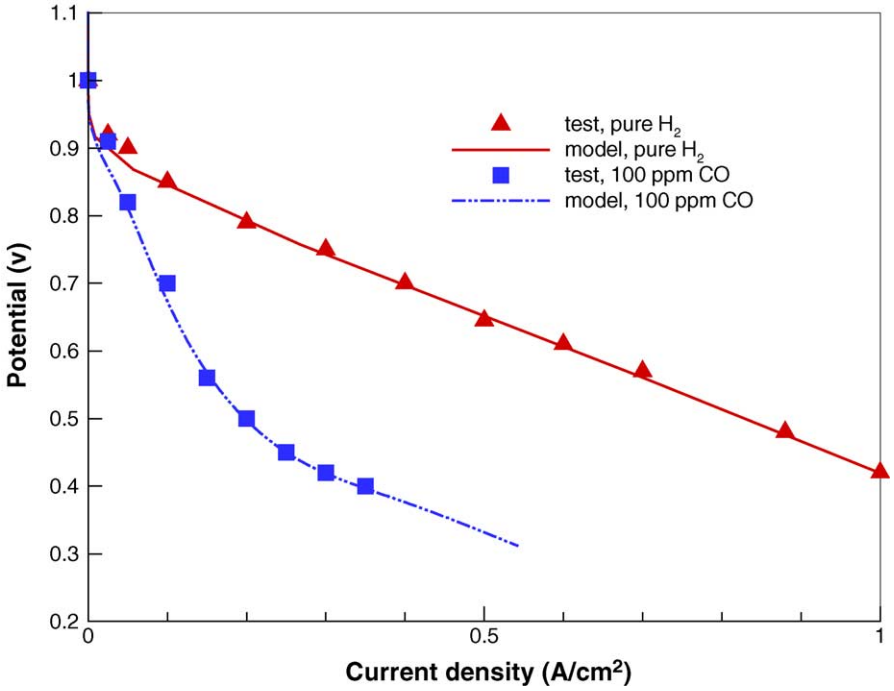

Fig. 13. Comparison of modeling results with experimental data by Divisek et al. [19].

4. Conclusions

Based on our early fuel cell models, a three-dimensional mathematical model of PEM fuel cell operated on reformate is developed by incorporating the adsorption and oxidation kinetics of CO on platinum surface. This model is capable of studying the effect of CO poisoning as well as the effect of hydrogen dilution due to the inert gases. In this paper, presented are the simulation results of PEM fuel cell performances operating on reformate under various operating and design conditions. The following can be concluded based on the results of the 3D fuel cell model:

- If the anode stoichiometric ratio is not too low, fuel cell local current density increases along the flow direction. This is due to fact that down stream of the channel, the reduced CO poisoning effect is predominant over the effect of hydrogen concentration reduction.
- With enough hydrogen supply, fuel cell performance increases with decreasing anode flow rate.
- In the regular range, fuel cell performance increases with the decrease of anode GDL porosity. The optimal GDL porosity is much lower for fuel cell using reformate than using pure hydrogen.
- There is an optimal value for the width of the collector plate shoulder. Usually, when contact resistance is neglected, the narrower the width the better the fuel cell performance, but for fuel cell using reformate, this is not the case due to the opposite effects of CO poising and reduction in hydrogen concentration.

The modeling results demonstrated the uniqueness of 3D models over 1D and 2D models. The results from the 3D model have revealed new phenomena that cannot be predicted by the previous 1D or 2D models. Please note that the modeling results depend on the design and operating parameters and could be different from any specific set of experimental results. Furthermore, the core of the 3D model is independent of the kinetic models, and any new kinetic models can be easily incorporated into the 3D model for better results or for different catalysts such as Pt/Ru. The model can also be extended to incorporate effects of other CO poisoning reduction effects, such as air bleed, provided appropriate kinetics models are available.

Acknowledgements

The financial support of the US Department of Energy's CARAT program under contract DE-FC02-98EE50531 is gratefully acknowledged.

References

[1] T. Zhou, H.T. Liu, Int. J. Transport Phenomena 3 (2001) 177–198.
[2] T.E. Springer, T.A. Zawodzinski, S. Gottesfeld, Proceedings of the Electrochemical Society, Montreal, Canada, 1997.
[3] T.E. Springer, T. Rockward, T.A. Zawodzinski, J. Electrochem. Soc. 148 (2001) A11–A23.
[4] T. Zhou, H.T. Liu, Prog. Comput. Fluid Dyn. 2 (2002) 97–105.
[5] W. He, J. Yi, T.V. Nguyen, AIChE 46 (2000) 2053–2064.
[6] A. Kazim, H.T. Liu, P. Forges, J. Appl. Electrochem. 29 (1999) 1409–1416.
[7] T.R. Ralph, G.A. Hards, J.E. Keating, S.A. Campell, D.P. Wilkinson, M. Davis, J. St-Pierre, M.C. Johnson, J. Electrochem. Soc. 144 (1997) 3845–3857.
[8] M. Ciureanu, H. Wang, J. Electrochem. Soc. 146 (1999) 4031–4040.
[9] C. He, H.R. Kunz, J.M. Fenton, J. Electrochem. Soc. 148 (2001) A1116–A1124.
[10] I. Son, M. Shamsuzzoha, A. Lane, J. Catal. 210 (2002) 460–465.
[11] L.P.L. Carrette, K.A. Friedrich, M. Huber, U. Stimming, Phys. Chem. 3 (2001) 320–324.
[12] S.J. Lee, S. Mukerjee, E.A. Ticianelli, J. McBreen, Electrochim. Acta 44 (1999) 3283–3293.
[13] J.-D. Kim, Y.-I. Park, K. Kobayashi, M. Nagai, J. Power Sour. 103 (2001) 127–133.
[14] H. Igarashi, T. Fujino, Y. Zhu, et al., Phys. Chem. 3 (2001) 306–314.
[15] G.A. Camara, E.A. Ticianelli, S. Mukerjee, S.J. Lee, J. McBreen, J. Electrochem. Soc. 149 (2002) A748–A753.
[16] U. Koponen, T. Peltonen, M. Bergelin, T. Mennola, M. Valkiainen, J. Kaskimies, M. Wasberg, J. Power Sour. 86 (1986) 261–268.
[17] A.T. Haug, R.E. White, J.W. Weidner, W. Huang, J. Electrochem. Soc. 149 (2002) A862–A867.
[18] A.T. Haug, R.E. White, J.W. Weidner, W. Huang, S. Shi, N. Rana, S. Grunow, T.C. Stoner, A.E. Kaloyeros, J. Electrochem. Soc. 149 (2002) A868–A872.
[19] J. Divisek, H.-F. Oetjen, V. Peinecke, V.M. Schmidt, Electrochim. Acta 43 (1998) 3811–3815.
[20] H.F. Oetjen, V.M. Schmidt, U. Stimming, F. Trila, J. Electrochem. Soc. 143 (1996) 3838–3842.
[21] J. Zhang, T. Thampan, R. Datta, J. Electrochem. Soc. 149 (2002) A765–772.
[22] V. Gurau, H.T. Liu, S. Kakac, AIChE 44 (1998) 2410–2422.
[23] A. Parthasarathy, S. Srinivasan, A.J. Appleby, J. Electrochem. Soc. 139 (1992) 2530–2537.